nature nanotechnology

Article

https://doi.org/10.1038/s41565-022-01312-z

Electrically switchable anisotropic polariton propagation in a ferroelectric van der Waals semiconductor

Received: 9 January 2022

Accepted: 14 December 2022

Published online: 23 January 2023

Check for updates

Yue Luo[1,2,9], Nannan Mao[3,9], Dapeng Ding[2,4], Ming-Hui Chiu[3,5], Xiang Ji[3], Kenji Watanabe[6], Takashi Taniguchi[7], Vincent Tung[5,8], Hongkun Park[2,4], Philip Kim[2], Jing Kong[3] & William L. Wilson[1]

Tailoring of the propagation dynamics of exciton-polaritons in two-dimensional quantum materials has shown extraordinary promise to enable nanoscale control of electromagnetic fields. Varying permittivities along crystal directions within layers of material systems, can lead to an in-plane anisotropic dispersion of polaritons. Exploiting this physics as a control strategy for manipulating the directional propagation of the polaritons is desired and remains elusive. Here we explore the in-plane anisotropic exciton-polariton propagation in SnSe, a group-IV monochalcogenide semiconductor that forms ferroelectric domains and shows room-temperature excitonic behaviour. Exciton-polaritons are launched in SnSe multilayer plates, and their propagation dynamics and dispersion are studied. This propagation of exciton-polaritons allows for nanoscale imaging of the in-plane ferroelectric domains. Finally, we demonstrate the electric switching of the exciton-polaritons in the ferroelectric domains of this complex van der Waals system. The study suggests that systems such as group-IV monochalcogenides could serve as excellent ferroic platforms for actively reconfigurable polaritonic optical devices.

Materials strategies for manipulating optical fields at the nanoscale are an important priority as we develop new technologies for integrated nanophotonic systems and devices. The van der Waals (vdW) materials offer a unique atomically thin platform for creating deterministic, advanced material functions, enabling a new design space for nanophotonic and electronic systems[1–3]. Two-dimensional (2D) vdW materials have been shown to exhibit a wide variety of polaritonic physics depending on the nature of a particular system's electronic band structure[2]. Surface plasmon-polaritons in graphene[4,5] and hyperbolic phonon-polaritons in hexagonal-boron nitride (h-BN)[6,7] are among the most extensively studied systems, while exciton-polaritons (EPs) in transition metal dichalcogenides have been explored as well[8,9]. Polariton propagation is characterized by its dispersive transport behaviour associated with dielectric properties of the material. Recently, α-phase molybdenum trioxide (α-MoO_3) that supports in-plane anisotropic phonon-polaritons with elliptic and hyperbolic dispersion has been

[1]Center for Nanoscale Systems, Harvard University, Cambridge, MA, USA. [2]Department of Physics, Harvard University, Cambridge, MA, USA. [3]Department of Electrical Engineering and Computer Science, Massachusetts Institute of Technology, Cambridge, MA, USA. [4]Department of Chemistry and Chemical Biology, Harvard University, Cambridge, MA, USA. [5]Department of Material Science and Engineering, King Abdullah University of Science and Technology, Thuwal, Saudi Arabia. [6]International Center for Materials Nanoarchitectonics, National Institute for Materials Science, Ibaraki, Japan. [7]Research Center for Functional Materials Science, National Institute for Materials Science, Ibaraki, Japan. [8]Department of Chemical System Engineering, School of Engineering, The University of Tokyo, Tokyo, Japan. [9]These authors contributed equally: Yue Luo, Nannan Mao. e-mail: wwilson@cns.fas.harvard.edu

https://doi.org/10.1038/s41565-022-01312-z

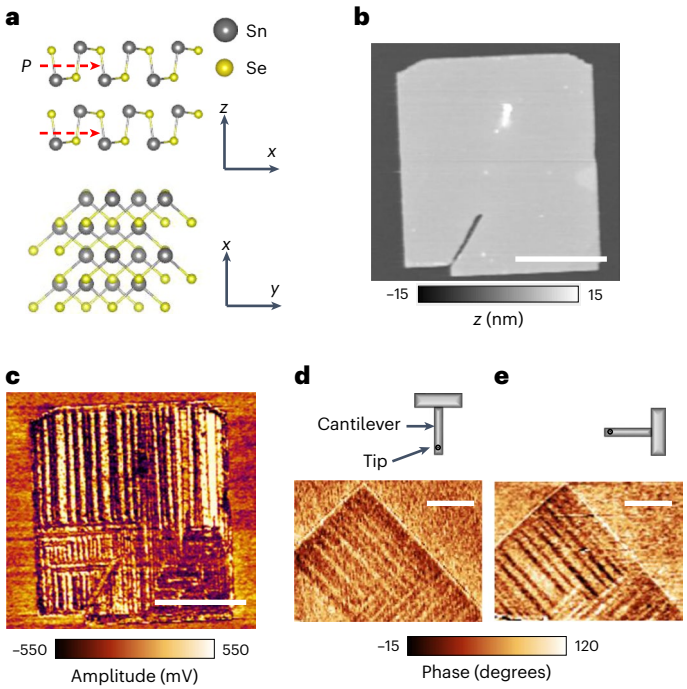

Fig. 1 | Abundant FE domains in the SnSe multilayer plate. a, Side (top panel) and top view (bottom panel) of geometric structures of the SnSe compound in the layered *Pnma*. Red arrows indicate the direction of the spontaneous polarization *P* of each layer. **b**, An AFM image of the SnSe plate with thickness of 9 nm. Scale bar, 4 µm. **c**, A LPFM amplitude image of the FE domains. Scale bar, 4 µm. **d**,**e**, LPFM phase images of the FE domains. The domains are oriented along the diagonal direction of the *xy* scanning axes. The long axis of the AFM cantilever is oriented along the vertical (**d**) and horizontal (**e**) directions, respectively. Cantilever orientations are shown as schematics in the top of **d** and **e**. Scale bar, 1 µm. All measurements were performed at room temperature.

reported[10,11]. Using this property as a practical active device development strategy however, would be challenging, since only fixed selection of the slab thickness has been shown to tune the phonon-polaritons in α-MoO_3 (ref. 10). Dynamic control of the polariton dispersion is the key to a range of integrated planar photonic device applications.

Fortunately, anisotropic dielectric properties are common in polar materials such as ferroelectric (FE) materials that naturally support different spontaneously polarized states below the Curie temperature[12]. Moreover, layered vdW FE materials, such as SnTe (ref. 13), SnS (ref. 14), In_2Se_3 (ref. 15) WTe_2 (ref. 16) and so on, have been discovered in recent years and offer an attractive platform for building multifunctional nanoelectronics[17]. The polarized states in these materials are probably switchable with application of an electric field[12,18] to dynamically tune the dispersion of the polaritons propagating in FE domains. The potential ability to control optical confinement using tuneable anisotropic dispersion in natural vdW materials can lead to reconfigurable polariton optics.

Monolayer and multilayer SnSe, a group-IV monochalcogenide semiconductor, exhibits in-plane ferroelectricity with strong spontaneous polarization[18,19]. In addition, this system supports an excitonic state at room temperature with a predicted large binding energy up to 300 meV for a monolayer[20] and roughly 50 meV for multilayers[21]. Here we report exploring in-plane EP with unique interplay of material properties in SnSe multilayer plates and control of dispersion through FE domain switching. We show that these domains can be imaged optically at the nanoscale with high spatial resolution scattering-type scanning near-field optical microscopy (s-SNOM). We experimentally demonstrate the in-plane anisotropy of the EP dispersive propagation in these FE domains by real-space nano-imaging. Moreover, by applying external electric field with electrodes, we demonstrate that dispersion behaviour and amplitude contrast of EPs can be tuned by switching the FE spontaneous polarization. In-plane anisotropic EP in vdW FE materials could become a promising platform for actively switchable on-chip polaritonic devices to obtain variable distributions of effective indexes in space.

We first characterize the in-plane FE domain structure of the physical vapour deposition (PVD) -grown SnSe plates with lateral piezoresponse force microscopy (LPFM) (Methods). Bulk SnSe crystalizes in a layered orthorhombic structure with the *Pnma* space group at room temperature. Figure 1a illustrates the schematic side and top view of ferroelectrically coupled SnSe layers along the armchair crystallographic direction (*x* axis). The in-plane spontaneous polarization *P* observed is parallel to the armchair direction, and results from the natural geometric distortion between the Sn and Se atoms in the puckered sheet[19]. A topography image of a typical SnSe multilayer plate recorded by atomic force microscopy (AFM) is shown in Fig. 1b. The side length of the SnSe plates can reach tens of micrometres. To reveal the in-plane FE domains, LPFM simultaneously records the lateral torsion force of the biased cantilever during the scanning[22]. The LPFM amplitude image of the SnSe plate shows abundant domains with bright–dark contrast (Fig. 1c). Multilayer SnSe plates have predominantly 90° domain walls in contrast to the 180° domain walls observed in SnSe monolayer plates[18]. This difference is probably related to the layer stacking or thickness of the SnSe plates and the inter-layer crystal growth dynamics. We confirm the domain orientation angles by imaging the sample under different scanning directions with respect to the AFM cantilever (Fig. 1d). Since *P* is either parallel or perpendicular to the lattice vector, we rotate the sample by 90° and observe the flipping of bright–dark contrast (Fig. 1e). The crystal structural change in the domain formation is checked by scanning transmission electron microscopy imaging of the cross-section of a SnSe plate (Supplementary Notes 1).

After characterizing the FE domain structures of the SnSe plates, we investigate the polariton-driven near-field optical response in this system using an s-SNOM as sketched in Fig. 2a. A metal coated AFM tip acts as the near-field optical probe. The tip is illuminated by continuous-wave lasers tuned across several frequencies in the visible and near-infrared range (Methods). The metallic AFM tip with small radius strongly enhances the local electric field between the tip and the sample, and the induced optical field response is highly sensitive to the material permittivity and the underlying polarization[23]. Instead of measuring the torsion of a cantilever from material deformation induced by the electric field applied through a tip as in LPFM, s-SNOM measures the amplitude and phase of scattered photons that are modified by the tip-enhanced light–material interaction.

We first explore the excitonic nature of SnSe multilayer plates using photoluminescence spectroscopy and optical reflectivity measurements at room temperature (Fig. 2b). Bulk SnSe at room temperature has a bandgap energy reported to be 0.86 eV (ref. 24), while monolayer SnSe has a bandgap of 2.13 eV at 1.8 K (ref. 18). The reflectance contrast indicates a broad excitonic resonance energy round 1.45 eV, while the photoluminescence spectrum shows relaxed emission energy at 1.4 eV. This finding is in line with the exciton binding energy predicted to be about 50 meV (refs. 21, 25), comparable to bulk transition metal dichalcogenides[26]. We also measured the photoluminescence intensity as a function of the laser excitation power (Fig. 2b and Supplementary Note 3). By fitting the data to the I–L^k law, we find the slope $k = 1.02$, which indicates that the photoluminescence emission has an origin of excitonic recombination[27]. By recording the scattered near-field amplitude $s(\omega)$ as a function of the tip position, we are able to map the FE domains in the SnSe plate (Fig. 2c). The domains with different *P* directions are identified with bright–dark contrast that probably originates from the optical conductivity variation under the linear polarized excitation. The dark regions in Fig. 2c are the domains

https://doi.org/10.1038/s41565-022-01312-z

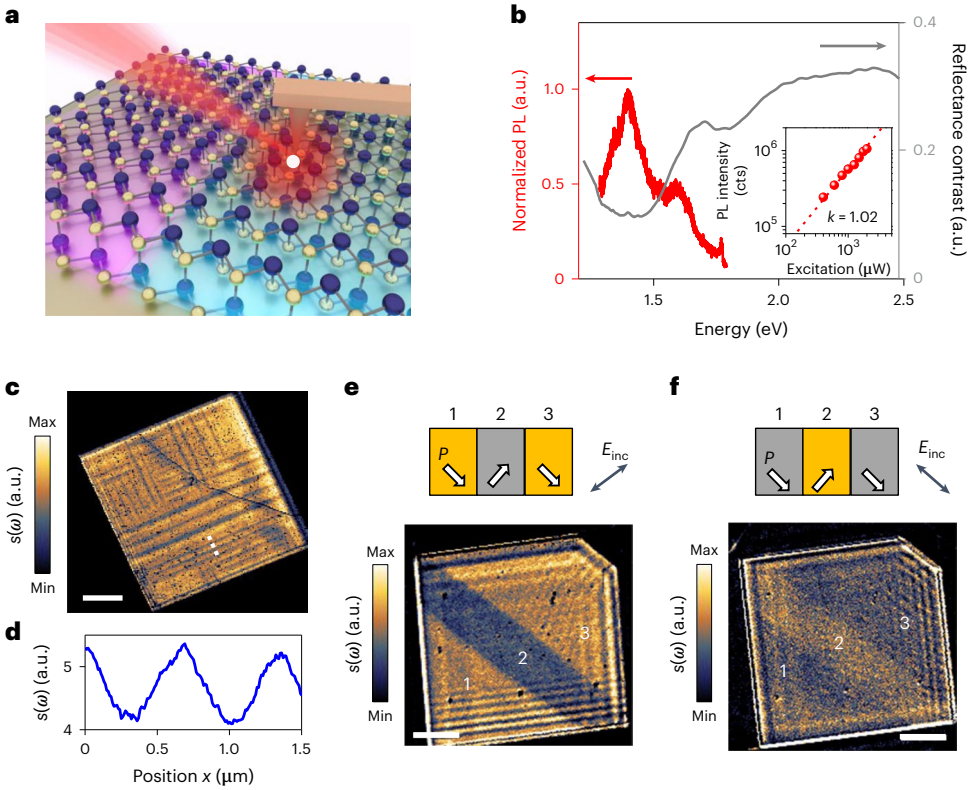

Fig. 2 | Near-field nano-imaging of the FE domains. a, Experimental schematic showing visible light beams incident and scattered by an AFM tip. The near-field response is detected through the scattered light in the far-field. **b**, Photoluminescence (PL) spectrum excited at laser energy $E = 1.88$ eV (red solid line) and reflectance contrast recorded with white light illumination (grey solid line). Inset shows the power dependence of the photoluminescence intensity. Red dashed line fits the data with fitted with I–L^k law. **c**, Near-field amplitude $s(\omega)$ in false colour maps revealing the FE domains in a SnSe multilayer plate with a thickness $d = 12$ nm taken at $E = 1.96$ eV. Scale bar, 2 μm. **d**, Cross-section profile taken at the white dashed line in **c**. **e**,**f**, Near-field images of the amplitude $s(\omega)$ with different polarization of the excitation light at $E = 1.96$ eV. Top panels show the schematics of the relations between the near-field amplitude $s(\omega)$, polarization of the excitation light and the spontaneous polarization of the domain. Bottom panels show the amplitude $s(\omega)$ with electric field E of the excitation light parallel to the direction of spontaneous polarization P_2 in **e** and parallel to P_1 and P_3 in **f**. The SnSe multilayer plate has a thickness of $d = 32$ nm. Scale bars, 2 μm.

that have smaller permittivity along the orientation of the in-plane component of the laser polarization: that is, P is parallel to the laser polarization (Methods). Accordingly, in the bright regions P is orthogonal to the laser polarization. We also compare the s-SNOM image of FE domains with LPFM on the same sample (Supplementary Note 2). The cross-section profile (Fig. 2d) indicates a strong bright–dark contrast with fringe visibility defined as $(s_{max} - s_{min})/s_{min}$ up to 26%. We note that imaging with excitation far from the resonance frequencies results in a 10–50 times smaller contrast (Supplementary Note 4). Commonly used imaging methods for FE domains, such as scanning tunnelling microscopy, piezoresponse force microscopy (PFM) and so on, generally require the AFM tip be in direct contact with the sample, thereby preventing any top protecting layer encapsulation. In the contrast, s-SNOM imaging with EP works well with the h-BN protection layer on top of the sample, since h-BN is transparent in the visible range[28] (Supplementary Note 5).

The underlying in-plane anisotropy of different FE domains shown above can be revealed by rotating the polarization of the excitation to be aligned to the spontaneous polarization orientation in each domain. As illustrated in the top panel of Fig. 2e, when the in-plane electric field of the incident laser beam E_i is parallel to the P of domains 1 and 3 but perpendicular to domain 2, the near-field amplitude of $s(\omega)$ of domain 1 and 3 is larger than $s(\omega)$ of domain 2. By 90° rotation of the in-plane E_i to parallel to the P of domain 2, the bright–dark contrast flipped (Fig. 2f). Such an exchange of the relative strength between the $s(\omega)$ of neighbouring domains matches the result from the LPFM and further confirms the existence of domain 90° walls that were absent in the SnSe monolayers. As predicted in the density function theory calculation[29], SnSe has strong natural in-plane anisotropy in the wavelength range between 1.55 and 2.48 eV (Supplementary Note 6).

We further studied EPs by real-space imaging of their propagating polariton dynamics through the interference fringes generated at different excitation energies. This nano-imaging method is a completely different approach compared to the conventional far-field spectroscopic approaches. Here the excitation or detection energy is fixed and a large range of momentum can be accessed due to the extremely small mode volume excited by coupling to the AFM tip[8]. Figure 3a–c shows near-field imaging near the edge of the samples at different laser excitation energy E where the interference fringes serve as a direct measure of the energy dispersion at a fixed material thickness. We extract line traces perpendicular to the edge and plotted in Fig. 3d–f. The fringe periods (ρ) are extracted by fitting the experimental $s(\omega)$ line profiles with a damped sinusoidal function (Methods). The EP wavelength (λ_{ep}) can be quantitatively analysed by evaluating the measured fringe ρ of the bright fringes and calibrating with the incident angle of the laser beam relative to the sample surface[8,9] $\frac{\lambda_0}{\rho} \approx \frac{\lambda_0}{\lambda_{ep}} - \cos\alpha$, where α is the incident angle. The fringe period shown in Fig. 3d is about 355 nm, so the wavelength of the EP is $\lambda_{ep} = 225$ nm at the laser energy $E = 2.33$ eV. The confinement ratio of the EP in this SnSe multilayer plate

https://doi.org/10.1038/s41565-022-01312-z

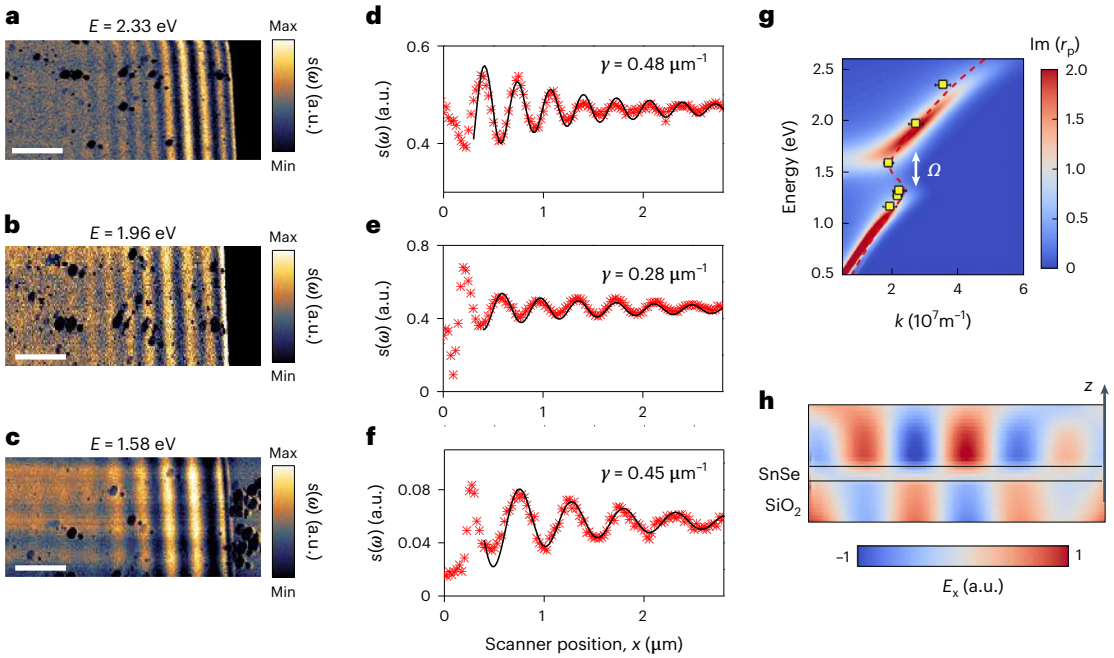

Fig. 3 | Near-field nano-imaging of EPs on SnSe. a–**c**, Near-field amplitude image of EPs on a $d = 52$ nm SnSe plate with various excitation energies of 2.33 eV (**a**), 1.96 eV (**b**) and 1.58 eV (**c**). Scale bars, 1 μm. **d**–**f**, s-SNOM line traces taken in **a**–**c** (red crosses). Damped sinusoidal functions (black solid lines) were fitted to the data with damping rate $\gamma = 0.48\ \mu m^{-1}$ (**d**), $\gamma = 0.28\ \mu m^{-1}$ (**e**) and $\gamma = 0.45\ \mu m^{-1}$ (**f**). **g**, Dispersion of the EP modes in SnSe plates along the armchair direction. The colour plot is calculated using the Fresnel reflection coefficients $\mathrm{Im}(r_p)$. The red dashed line is the dispersion relation. Red squares are experimental data. **h**, Simulated near-field distribution of a EP mode propagating along the SnSe/SiO_2 layer.

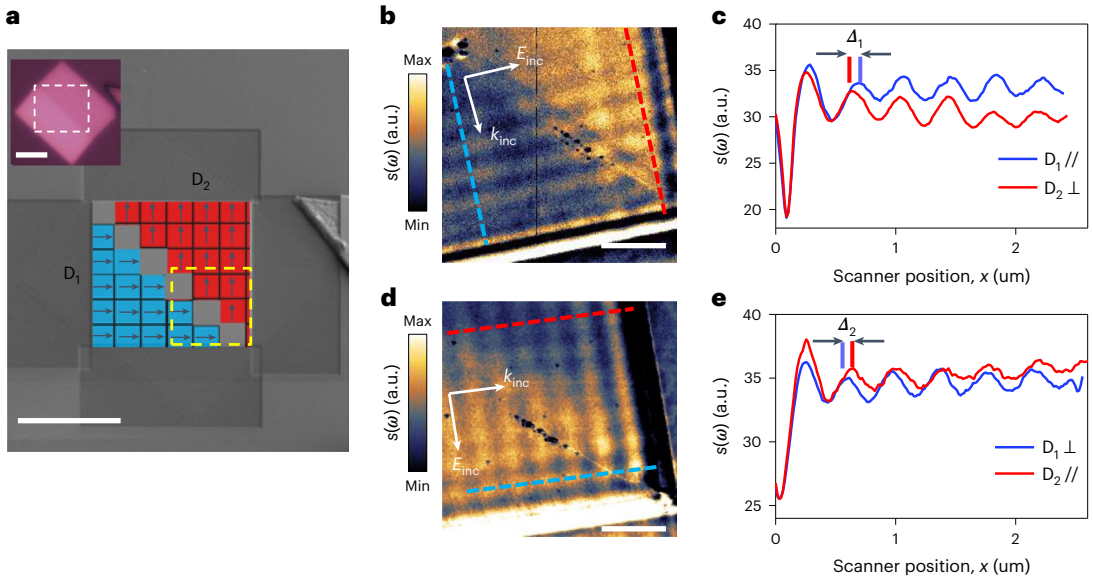

Fig. 4 | Anisotropy of EPs in SnSe. a, Scanning electron microscope image of the SnSe plate with thickness $d = 22$ nm, which has large FE domains and is etched by a focused ion beam. The schematic plot depicts possible arrangement of the domain wall (black solid line and grey squares) and polarization orientations (black arrows). Scale bar, 5 μm. Inset shows the polarized optical microscope image of the SnSe plate. The white dashed line marks the target shape of the etched plate. Scale bar, 2 μm. **b**,**d**, Near-field amplitude images of the EPs on SnSe with $E = 1.96$ eV excitation. By rotating the sample from 0° (**b**) to 90° (**d**), the orientation of the in-plane component of the electric field is rotated by 90° as illustrated with black double arrows. Scale bar, 500 nm. **c**,**e**, Line profiles taken in FE domains D_1 (blue line) and D_2 (red line) as marked by blue and red dashed lines that are perpendicular to the plate edge from **b** (plotted in **c**) and **d** (plotted in **e**), respectively. The shift of peak positions is marked as Δ_1 and Δ_2.

is defined to be $\lambda_0/\lambda_{ep} = 2.36$. We analyse the real-space images of the propagating EPs in the same SnSe plate at different excitation laser energies ($E = 1.96$ eV and $E = 1.58$ eV) to examine the dispersion relations of the EP. The corresponding EP wavelength is $\lambda_{ep} = 268$ nm at $E = 1.96$ eV and $\lambda_{ep} = 326$ nm at $E = 1.58$ eV using the same calibration, and the confinement ratios are 2.36 and 2.40, respectively. The fitted decay length

https://doi.org/10.1038/s41565-022-01312-z

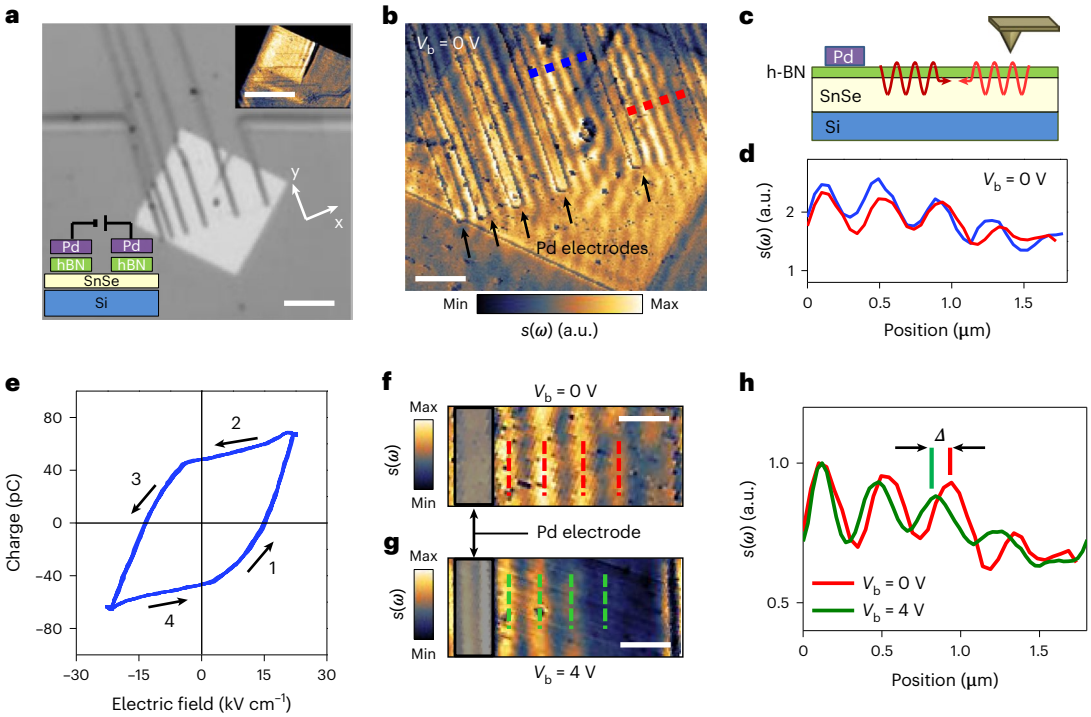

Fig. 5 | Electrically switching an EP in SnSe with metal electrodes. a, Optical microscope image of the device with Pd electrodes with channel widths of 400 to 2,000 nm. Scale bar, 5 μm. The top inset shows the near-field amplitude image of the SnSe plate before the device fabrication showing different FE domains. Scale bar, 5 μm. The bottom inset shows a schematic of the device stacking. **b**, Near-field amplitude image of the device before applying a bias voltage between electrodes (V_b = 0 V). Scale bar, 500 nm. **c**, Illustration of the propagating EPs launched by AFM tip and Pd electrode creating the fringes shown in **d**. Line profiles taken at blue and red dashed lines in **b**, respectively. **e**, FE polarization hysteresis loop of SnSe at room temperature with electric fields applied between the electrode at frequency f = 110 Hz. **f**,**g**, A near-field amplitude image taken near the electrode (red dashed line region in **b**) with the in-plane electric field applied between the electrodes with a bias voltage V_b = 0 V (**f**) and V_b = 4 V (**g**). Red and green dashed lines mark the maximum of the fringes. Scale bars, 400 nm. **h**, Line profiles taken from **f** and **g** show the peak differences when FE polarization is switched by applying an electric field.

L_x for EP indicates that the polaritons have a propagation length of 2–8 μm, which is among the longest compared to EPs in other materials given the thin slab thickness (Supplementary Note 7). When excited near the resonance (E = 1.96 eV), the EP has the lowest loss factor $\gamma = 1/L_x = 0.28\ \mu m^{-1}$. To map the dispersion relation, we then carry out Fourier analysis on the real-space images of the polaritons by extracting line profiles directly from the images in Fig. 3a–c and performing one-dimensional fast Fourier transformation for the line profiles. The wave vector $\mathbf{k} = 2\pi/\rho$ can be determined by the inverse fringe period. In Fig. 3g, we demonstrate the dispersion relation of EPs propagating along the armchair direction by plotting experimental data points on the theoretical dispersion colour map. In the colour map, the imaginary part of the reflection coefficients Im(r_p) was plotted to represent the photonic density of states (Supplementary Note 8)[8,30]. The EP shows a clear anticrossing behaviour, which is a signature of strong coupling between the exciton and photonic waveguide mode. We estimate the Rabi splitting Ω of roughly 220 meV by extracting the minimal separation between the two branches of the dispersion[31], which is larger than the average polariton line width (roughly 90 meV) estimated by the mode broadening from the colour map. The finite-difference time domain near-field simulation shown in Fig. 3h reveals electric fields components of the propagating EP waveguide mode. The wavelength extracted from the simulation matches the experimental value from the interference fringes.

A key feature of SnSe is that the FE domains could be electrically tuned and offer intriguing options to manipulate the EPs propagation dynamics for future applications[18]. To explore this more rigorously when multiple domains exist, we need to map propagation purely along each unique polar axis. However, the pristine edges of the PVD synthesized SnSe plates are formed roughly 45° with respect to the crystal axis[18], resulting in an effective permittivity $\sqrt{\varepsilon_{xx}\varepsilon_{yy}}$. To quantitatively explore the manipulation of the EPs along the crystal axis of the domain, we use a SnSe multilayer plate with a large domain size (Fig. 4a). We engineer the sample by etching it with a focused ion beam so the edges of the plate are parallel to the zigzag or armchair directions (Fig. 4a). The resulting squarely structured SnSe plate contains the domain structure sketched in the colour scheme. We first excite the SnSe plate with laser polarization along the P of domain 1 (D_1) (Fig. 4b). Hence the permittivity for the EPs propagating in D_1 is ε_{yy} while in D_2 is ε_{xx}. We extract line profiles from the fringes only presented in a single domain (Fig. 4c). We find that the EPs propagating in D_1 have a wavelength of $\lambda_{ep1} = 398 \pm 5$ nm compared to propagating in D_2 with a wavelength of $\lambda_{ep2} = 378 \pm 4$ nm. The wavelength shift $\Delta_1 = \Delta\lambda_{ep}/\lambda_{ep} = 5.3 \pm 3\%$ indicates a strong modification on the EP dispersion in the FE domains. The propagation length L_x is fitted to be 8.5 ± 2 μm, indicating a low damping rate for near resonant excitation. To access the other optical axis in the same domain, we rotate the sample by 90° so the polarization of the incident laser beam is parallel to the P of D_2. As expected, the bright–dark contrast between D_1 and D_2 exchange in relative strength of the detected $s(\omega)$ (Fig. 4d), in good agreement with Fig. 2d,e. We again extract line profiles to at each domain (Fig. 4e) and find that EPs in D_1 now have shorter wavelengths than that propagating in D_2 with $\lambda_{ep1} = 380 \pm 4$ and $\lambda_{ep2} = 398 \pm 4$ nm, yielding $\Delta_2 = 4.7 \pm 2\%$. The anisotropic behaviour is also investigated at other energies (Supplementary Note 9). The demonstrated domain related change in EP wavelength suggests the potential for reversible tuneability via control of the FE spontaneous polarization.

https://doi.org/10.1038/s41565-022-01312-z

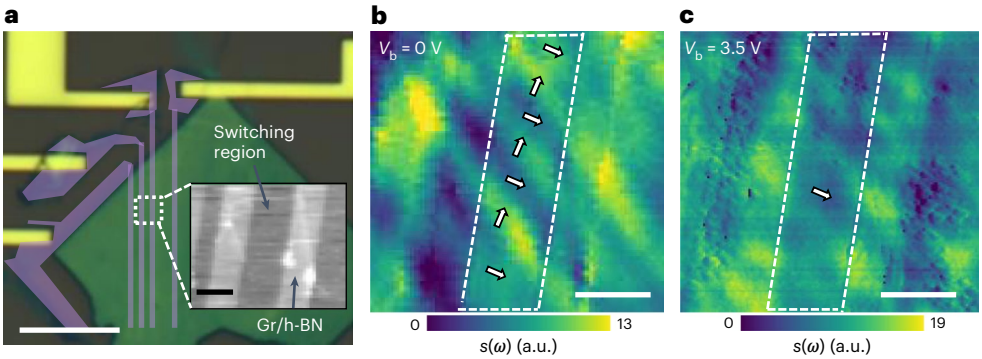

Fig. 6 | Electrically switching an EP in SnSe with graphene/h-BN electrodes. **a**, Optical microscope image of the device with graphene electrodes shown in purple as a false colour. Scale bar, 5 µm. Inset shows AFM topography image of graphene electrodes on the SnSe plate with 400 nm channel width. Scale bar, 400 nm. **b**, Near-field image of the switching region (white dashed line) with applied bias voltage V_b = 0 V between the electrodes. Arrows represent the FE polarization in the different domains. Scale bar, 400 nm. **c**, Near-field image of the switching region with a bias voltage V_b = 3.5 V between the electrodes. The bright–dark contrast in the switching region has been dramatically reduced. The arrow indicates the aligned FE polarization parallel to the electric field. Scale bar, 400 nm.

For out-of-plane FE materials, switching spontaneous polarization can be effectively realized by tip poling with a scanning-probe microscope[22]. However, it is more difficult to switch in-plane FEs since the direction of the in-plane component of the electric field applied by the AFM tip cannot be simply controlled. To demonstrate electrically switchable EPs in SnSe, we fabricated a switching device (dev1) with Pd/Cr electrodes that cover different domains and align with the crystal axis (Fig. 5a). In addition to applying an electric field, metal electrodes are used here as antenna to launch an EP that can interfere with the tip-launched EP and generate fringes (Fig. 5b,c). The electrode-launched EP propagating in different domains also shows a wavelength difference with a bias voltage of V_b = 0 V (Fig. 5d). We analyse the switching behaviour quantitatively by measuring the FE polarization versus the electric field through the total charge (Q). Note that since the leakage current is relatively large, the change of Q may not solely come from the displacement current. Figure 5e shows a distinct hysteresis loop when an a.c. bias at 110 Hz was applied and cycled (0 → +4 → −4 → 0 V), which is direct evidence of ferroelectricity in multilayer SnSe. To confirm the underlying EP dispersion is also switched with the electric field, we image the EP interference fringes after applying a different bias voltage. A clear shift is observed in the fringe positions when comparing the $s(\omega)$ images taken at the same location with a bias voltage of V_b = 0 V (Fig. 5f) and above the saturation voltage at V_b = 4 V (Fig. 5g), indicating that the λ_{ep} changed with the switching of the P. We analyse the line profile taken from Fig. 5f,g and find that $\lambda_{ep1} = 405 \pm 5$ and $\lambda_{ep2} = 362 \pm 5$ nm at 0 and 4 V, respectively, yielding $\Delta = 11.9 \pm 3\%$ (Fig. 5h). The difference of λ_{ep} is even larger than that in the different pristine domains possibly due to a better aligned P between each layer.

To directly visualize the domain structure change without generating fringes, we used graphene as the electrode material on a different device (dev2). The change of domain structure is observed using the EP amplitude contrast (Fig. 6a). Similar to the dev1, we etched graphene electrodes with channel widths of 200 to 800 nm. In particular, dev2 has abundant domains so the switching region contains different FE domains that have 90° domain walls showing a bright–dark contrast (Fig. 6b). When the in-plane electric field is applied between the electrodes with a bias voltage V_b = 3.5 V, above the coercive field, P of domains that were perpendicular to the electric field, that is the bright domains shown in Fig. 6b, are switched to be parallel to the electric field. Therefore, the $s(\omega)$ image shows a strongly reduced bright–dark contrast in the switching region (Fig. 6c). We also extracted the line profile from Fig. 6b,c to evaluate the amplitude contrast difference (Supplementary Note 10). Propagating EPs launched and detected by s-SNOM act as promising platforms for ultrasensitive on-chip spectroscopy at the nanoscale.

The anisotropic EP propagation in SnSe multilayer plates reveals a unique interplay between photons and excitons in SnSe, as well as its in-plane FE domains. The enhanced light-mater interaction enables s-SNOM as a powerful tool for imaging the microscopic domain structures in FE materials. In contrast to the conventional detection method such as PFM and scanning tunnelling microscopy, s-SNOM imaging has fewer restrictions on the substrate material of the target sample and the sample can be encapsulated with protection layers[32]. In addition, the FE domains combined with appropriate external stimuli can be used as an effective platform to actively tune the anisotropic polariton properties. With proper design and pattered nanostructure arrays, enabling far-field excitation and probing is feasible for on-chip polariton sensing or focusing devices[33–35]. Furthermore, with optimized crystal growth to increase the SnSe plate size and FE stacking order, this material platform allows potential integration of optical devices in numerous applications ranging from optical phased arrays and optical switching platforms to quantum network components.

Online content

Any methods, additional references, Nature Portfolio reporting summaries, source data, extended data, supplementary information, acknowledgements, peer review information; details of author contributions and competing interests; and statements of data and code availability are available at https://doi.org/10.1038/s41565-022-01312-z.

References

1. Basov, D. N., Fogler, M. M. & de Abajo, F. J. G. Polaritons in van der Waals materials. *Science* **354**, aag1992 (2016).
2. Zhang, Q. et al. Interface nano-optics with van der Waals polaritons. *Nature* **597**, 187–195 (2021).
3. Low, T. et al. Polaritons in layered two-dimensional materials. *Nat. Mater.* **16**, 182–194 (2016).
4. Fei, Z. et al. Gate-tuning of graphene plasmons revealed by infrared nano-imaging. *Nature* **487**, 82–85 (2012).
5. Chen, J. et al. Optical nano-imaging of gate-tunable graphene plasmons. *Nature* **487**, 77–81 (2012).
6. Dai, S. et al. Tunable phonon polaritons in atomically thin van der Waals crystals of boron nitride. *Science* **343**, 1125–1129 (2014).

7. Caldwell, J. D. et al. Sub-diffractional volume-confined polaritons in the natural hyperbolic material hexagonal boron nitride. *Nat. Commun.* **5**, 5221 (2014).
8. Hu, F. et al. Imaging exciton–polariton transport in $MoSe_2$ waveguides. *Nat. Photonics* **11**, 356–360 (2017).
9. Fei, Z. et al. Nano-optical imaging of WSe_2 waveguide modes revealing light-exciton interactions. *Phys. Rev. B.* **94**, 081402 (2016).
10. Ma, W. et al. In-plane anisotropic and ultra-low-loss polaritons in a natural van der Waals crystal. *Nature* **562**, 557–562 (2018).
11. Zheng, Z. et al. A mid-infrared biaxial hyperbolic van der Waals crystal. *Sci. Adv.* **5**, eaav8690 (2019).
12. Martin, L. W. & Rappe, A. M. Thin-film ferroelectric materials and their applications. *Nat. Rev. Mater.* **2**, 16087 (2016).
13. Chang, K. et al. Discovery of robust in-plane ferroelectricity in atomic-thick SnTe. *Science* **353**, 274–278 (2016).
14. Higashitarumizu, N. et al. Purely in-plane ferroelectricity in monolayer SnS at room temperature. *Nat. Commun.* **11**, 2428 (2020).
15. Xiao, J. et al. Intrinsic two-dimensional ferroelectricity with dipole locking. *Phys. Rev. Lett.* **120**, 227601 (2018).
16. Fei, Z. et al. Ferroelectric switching of a two-dimensional metal. *Nature* **560**, 336–339 (2018).
17. Wu, M. Two-dimensional van der Waals ferroelectrics: scientific and technological opportunities. *ACS Nano* **15**, 9229–9237 (2021).
18. Chang, K. et al. Microscopic manipulation of ferroelectric domains in SnSe monolayers at room temperature. *Nano Lett.* **20**, 6590–6597 (2020).
19. Fei, R., Kang, W. & Yang, L. Ferroelectricity and phase transitions in monolayer group-IV monochalcogenides. *Phys. Rev. Lett.* **117**, 097601 (2016).
20. Shi, G. & Kioupakis, E. Anisotropic spin transport and strong visible-light absorbance in few-layer SnSe and GeSe. *Nano Lett.* **15**, 6926–6931 (2015).
21. Meléndez, J. J., González-Romero, R. L. & Antonelli, A. Quasiparticle bands and optical properties of SnSe from an ab initio approach. *Comp. Mater. Sci.* **152**, 107–112 (2018).
22. Gruverman, A., Alexe, M. & Meier, D. Piezoresponse force microscopy and nanoferroic phenomena. *Nat. Commun.* **10**, 1661 (2019).
23. Keilmann, F. & Hillenbrand, R. Near-field microscopy by elastic light scattering from a tip. *Philos. Trans. R. Soc. A.* **362**, 787–805 (2004).
24. Zhao, L.-D. et al. Ultralow thermal conductivity and high thermoelectric figure of merit in SnSe crystals. *Nature* **508**, 373–377 (2014).
25. Nguyen, H. T. et al. Temperature dependence of the dielectric function and critical points of -SnS from 27 to 350 K. *Sci. Rep.* **10**, 18396 (2020).
26. Beal, A. R., Knights, J. C. & Liang, W. Y. Transmission spectra of some transition metal dichalcogenides. II. Group VIA: trigonal prismatic coordination. *J. Phys. C. Solid State Phys.* **5**, 3540–3551 (1972).
27. Schmidt, T., Lischka, K. & Zulehner, W. Excitation-power dependence of the near-band-edge photoluminescence of semiconductors. *Phys. Rev. B* **45**, 8989–8994 (1992).
28. Cassabois, G., Valvin, P. & Gil, B. Hexagonal boron nitride is an indirect bandgap semiconductor. *Nat. Photonics* **10**, 262–266 (2016).
29. Zhou, J., Zhang, S. & Li, J. Normal-to-topological insulator martensitic phase transition in group-IV monochalcogenides driven by light. *NPG Asia Mater.* **12**, 2 (2020).
30. Hu, F. et al. Imaging propagative exciton polaritons in atomically thin WSe_2 waveguides. *Phys. Rev. B.* **100**, 121301 (2019).
31. Kockum, A. F., Miranowicz, A., Liberato, S. D., Savasta, S. & Nori, F. Ultrastrong coupling between light and matter. *Nat. Rev. Phys.* **1**, 19–40 (2019).
32. Luo, Y. et al. In situ nanoscale imaging of moiré superlattices in twisted van der Waals heterostructures. *Nat. Commun.* **11**, 4209 (2020).
33. Rodrigo, D. et al. Mid-infrared plasmonic biosensing with graphene. *Science* **349**, 165–168 (2015).
34. Autore, M. et al. Boron nitride nanoresonators for phonon-enhanced molecular vibrational spectroscopy at the strong coupling limit. *Light. Sci. Appl.* **7**, 17172 (2017).
35. Hu, H. et al. Far-field nanoscale infrared spectroscopy of vibrational fingerprints of molecules with graphene plasmons. *Nat. Commun.* **7**, 12334 (2016).

Methods

SnSe sample preparation

Tin monoselenide (SnSe) was synthesized onto mica substrate via PVD. SnSe power (99.999%, Alfa Aesar) was used as a precursor. It was placed in a quartz boat and then placed in the centre of a 1-inch furnace. A freshly exfoliated mica substrate was annealed at 400 °C in air for 30 min before it was sent downstream of the furnace. Thereafter, the PVD system was pumped down by the mechanical pump to 10 mTorr with a leakage rate of less than 20 mTorr min^{-1}. The furnace was then heated up to 420 °C with a ramping speed of 40 °C min^{-1} and carrier gases of 65 sccm Ar and 5 sccm H_2. The synthesis was continued for 30 min and the furnace was then quickly cooled down by opening the cap and fan until it reached room temperature.

LPFM measurement

The LPFM measurements were performed on a commercial AFM (Cypher S, Asylum Research). We used a conducting AFM tip coated with Pt/Ir tuned around 300 kHz for the vertical response and 750 kHz for the lateral response. Using the vector PFM mode, the polarization state can be determined by measuring the lateral amplitude and phase of the piezoelectric vibration signal due to the bias-induced piezoelectric surface deformation. We scan the sample surface in the direction perpendicular to the cantilever axis so the presence of the piezoresponse component along the cantilever is minimized. The in-plane tip displacement is detected by the photodetector through the laser deflection on the cantilever. The domain orientation angles are determined by imaging the sample under different scanning directions with respect to the AFM cantilever orientation that changes the torsion direction and therefore the force detected.

Photoluminescence and reflectance spectroscopy

Photoluminescence measurement was performed at room temperature with a Montana Instruments system. For optical excitation, we used a single-line laser diode operating at 660 nm in continuous-wave mode. Reflectivity measurement was performed at room temperature with a Horiba XploRa system. We used a perpendicular incidence excitation with a tungsten-halogen white light source filtered by a broadband linear polarizer. Reflected light from the sample on a SiO_2/Si substrate was collected by a ×100 microscope objective and sent through a spectrometer with a CCD camera to generate hyperspectral mapping of the sample. The reflectance contrast is calculated as $(R_{sample} - R_{sub})/R_{sub}$.

Near-field optical measurement

The nano-imaging experiments were performed using s-SNOM (Attocube systems AG). The system is equipped with solid state lasers at 532, 633, 784, 940, 976 and 1,064 nm for nano-imaging at visible range and quantum-cascade laser for the mid-infrared range. The polarization of the laser beam is controlled via a broadband half-wave plate placed in the incident beam path. The platinum silicon coated tip used in the s-SNOM has a typical radius of 20 nm operating in the tapping mode with a tapping frequency around 240 kHz. We use pseudo-heterodyne interferometric detection module to extract the near-field signal. The background signal is suppressed by demodulation of the near-field signal at the third harmonics of the tapping frequency. All the near-field optical measurements are done at room temperature.

We can simply model the SnSe layer as an anisotropic in-plane conducting layer with an effective 2D optical conductivity tensor $\hat{\sigma}_{eff} = (cd/2i\lambda_0)\hat{\varepsilon}$, where d is the layer thickness, λ_0 is the wavelength of the excitation light and $\hat{\varepsilon} = \mathrm{diag}(\varepsilon_{xx}, \varepsilon_{yy})$ is the in-plane permittivity tensor[10]. It is predicted by density function theory calculations[29], that both the real and imaginary parts of the permittivity in armchair direction (ε_{xx}) are smaller than the permittivity in the zigzag direction (ε_{yy}), within the energy range explored here.

We quantitatively analyse the anisotropic EP propagation by fitting the s-SNOM amplitude line profile with an exponentially decaying sinusoidal function: $y = Ae^{-x/L_x}\sin(2\pi x/\rho - B) + C$, where L_x is the decay length and A, B and C are fitting parameters. In the fitting process, we achieved convergence criteria of the Levenberg–Marquardt algorithm.

Device fabrication and transport measurements

The devices used for domain switching are fabricated using polycarbonate dry transfer techniques and electron beam lithography. For device 1, a 4.8-nm-thick h-BN flake is transferred onto a SnSe flake on a silicon substrate. Parallel electrodes are fabricated using 2 nm Cr and 35 nm Pd. The electrodes are 200 nm wide and are separated by 400, 800, 1,200, 2,000 and 2,000 nm, respectively. For device 2, graphene (three layers) and h-BN (2.2 nm thick) flakes are picked up subsequently, and then transferred onto a SnSe flake on a silicon substrate. The graphene flake is patterned into parallel electrodes by using a poly(methyl methacrylate) mask and reactive ion etching of O_2 plasma. The electrodes are 500 nm wide. The spacings between the electrodes are 200, 500 and 800 nm, respectively. Contacts with the electrodes are made of 2 nm Cr and 48 nm Pd.

The electric polarization-induced charge versus electric field (Q-E) hysteresis loops are measured at room temperature. In-plane electric fields are applied between the electrodes using a function generator and the voltage over the reference capacitor (1 nF) is measured with a voltage amplifier and an oscilloscope.

Data availability

The data that support the plots within this paper and other finding of this study are available at the online depository Zenodo (https://doi.org/10.5281/zenodo.7395377).

Acknowledgements

We thank A. Akey and J. Gardener at the Centre for Nanoscale Systems (CNS) at Harvard University for the TEM sample preparation and imaging. We thank Y. Han at Rice University for the helpful discussion on the TEM results. Part of the work was performed at CNS support by the National Science Foundation (NSF) under award no. ECCS-2025158. Y.L. was supported by the US Department of Energy under award no. DE-SC0019300. N.M. and J.K acknowledge the support by the US Department of Energy, Office of Science, Basic Energy Sciences under award no. DE-SC0020042 and the support from the STC Center for Integrated Quantum Materials, NSF grant number DMR-1231319. X.J. and J.K. acknowledge the support from the US Army Research Office (ARO) MURI project under grant number W911NF-18-1-0432. D.D., H.P. and P.K. acknowledge support from US Air Force Office of Scientific Research grants (nos. FA2386-21-1-4086 for P.K. and FA9550-17-1-0002 for H.P.). H.P. and P.K. acknowledge support from Department of Defense Vannevar Bush Faculty Fellowship (grant nos. N00014-16-1-2825 for H.P. and N00014-18-1-2877 for P.K.), Samsung Electronics and the NSF (PHY-1506284 for H.P.)

Author contributions

Y.L., N.M. and W.L.W. conceived the experiment, Y.L., N.M., J.K. and W.L.W. planned the investigations. N.M., M.H-.C. and X.J. fabricated the pristine SnSe samples and carried out preliminary characterizations with J.K. and V.T. D.D. and Y.L. fabricated the device samples. Y.L. carried out the s-SNOM and LPFM experiments and analysed the data with N.M., J.K. and W.L.W. D.D. and Y.L. carried out the transport measurements under supervision of P.K. and H.P. Y.L. performed theoretical calculations and finite-difference time domain simulations. K.W and T.T provided the h-BN crystal. All authors discussed results and wrote the manuscript.

Competing interests

The authors declare no competing interests.

Additional information

Supplementary information The online version contains supplementary material available at https://doi.org/10.1038/s41565-022-01312-z.

Correspondence and requests for materials should be addressed to William L. Wilson.

Peer review information *Nature Nanotechnology* thanks Cheng-Wei Qiu and the other, anonymous, reviewer(s) for their contribution to the peer review of this work.